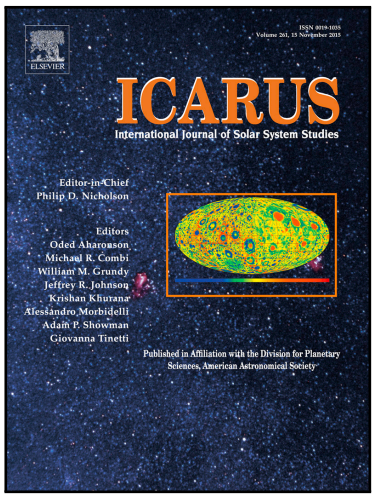

Sublimation Pit Distribution Indicates Convection Cell Surface Velocities of ~10 Centimeters per Year in Sputnik Planitia, Pluto

Peter B. Buhler , Andrew P. Ingersoll

PII: S0019-1035(16)30800-4
DOI: 10.1016/j.icarus.2017.09.018
Reference: YICAR 12614

To appear in: *Icarus*

Received date: 2 December 2016
Revised date: 6 September 2017
Accepted date: 11 September 2017

Please cite this article as: Peter B. Buhler , Andrew P. Ingersoll , Sublimation Pit Distribution Indicates Convection Cell Surface Velocities of ~10 Centimeters per Year in Sputnik Planitia, Pluto, *Icarus* (2017), doi: 10.1016/j.icarus.2017.09.018

Highlights

- We map 12,297 sublimation pits on 7 convection cells in Sputnik Planitia, Pluto
- We use an analytic model to calculate the growth rate, and thus ages, of the pits
- From the pit distribution we find surface convection rates and ages of the cells
- Growth rate: ~3.6 x 10^{-4} m/yr, Convection: ~1.5-17.9 cm/yr, Ages: ~4.2-8.9 x 10^{5} yr

Sublimation Pit Distribution Indicates Convection Cell Surface Velocities of ~10 Centimeters per Year in Sputnik Planitia, Pluto

Peter B. Buhler[a*], Andrew P. Ingersoll[a]

[a]*California Institute of Technology, Division of Geological and Planetary Science, Pasadena, CA, 91125, USA*

*Corresponding Author: *E-mail address:* bpeter@caltech.edu (P.B. Buhler)

Abstract.

The ~10^6 km^2 Sputnik Planitia, Pluto is the upper surface of a vast basin of nitrogen ice. Cellular landforms in Sputnik Planitia with areas in the range of a few × 10^2-10^3 km^2 are likely the surface manifestation of convective overturn in the nitrogen ice. The cells have sublimation pits on them, with smaller pits near their centers and larger pits near their edges. We map pits on seven cells and find that the pit radii increase by between 2.1 ± 0.4 × 10^{-3} and 5.9 ± 0.8 × 10^{-3} m per meter away from the cell center, depending on the cell. This is a lower bound on the size increase because of the finite resolution of the data. Accounting for resolution yields upper bounds on the size vs. distance distribution of between 4.2 ± 0.2 × 10^{-3} and 23.4 ± 1.5 × 10^{-3} m m^{-1}. We then use an analytic model to calculate that pit radii grow via sublimation at a rate of $3.6^{+2.1}_{-0.6} \times 10^{-4}$ m yr^{-1}, which allows us to convert the pit size vs. distance distribution into a pit age vs. distance distribution. This yields surface velocities between $1.5^{+1.0}_{-0.2}$ and $6.2^{+3.4}_{-1.4}$ cm yr^{-1} for the slowest cell and surface velocities between $8.1^{+5.5}_{-1.0}$ and $17.9^{+8.9}_{-5.1}$ cm yr^{-1} for the fastest cell. These convection rates imply that the surface ages at the edge of cells reach ~$4.2 - 8.9 \times 10^5$ yr. The rates are comparable to rates of ~6 cm yr^{-1} that were previously obtained from modeling of the convective overturn in Sputnik Planitia [McKinnon, W.B. et al., Nature, 534(7605), 82–85]. Finally, we investigate the surface rheology of the convection cells and estimate that the minimum ice viscosity necessary to support the geometry of the observed pits is of order 10^{16} – 10^{17} Pa s,

based on the argument that pits would relax away before growing to their observed radii of several hundred meters if the viscosity were lower than this value.

1. Introduction

The New Horizons mission revealed that Pluto is a geologically active planet with a dynamic surface (Stern et al., 2015; Moore et al., 2016a). In particular, the crater-free surface of Sputnik Planitia (SP, informal name)—which is thought to be the upper surface of a several-kilometer deep basin filled with nitrogen ice—is evidence that SP is < 10 Myr old (Greenstreet et al. 2015; Stern et al. 2015; Moore et al. 2016a). Cellular patterns in SP (Fig. 1, 2) have been interpreted as the upper surface of convection cells within the nitrogen ice that replenish the surface on the timescale of ~500,000 years (McKinnon et al., 2016; Trowbridge et al., 2016). Since there are no impact craters in SP, alternative methods are needed to independently date the surface.

Sublimation pits on the upper surface of SP (Moore et al. 2016a; Moore, et al. 2016b; White et al., 2017) provide such an alternative dating method. Cells in SP typically have smaller pits toward their centers and larger pits toward their edges (Fig. 1, 2; see also McKinnon et al. 2016; White et al. 2017), suggesting that the pits are growing larger by sublimation during transport from the centers to the edges of the convection cells. This motivates us to calculate the rate at which pit radii enlarge in order to use the spatial distribution of pit sizes to determine the surface velocity of the convection cells. We also determine the minimum viscosity required to support the pits. Finally, we discuss our results in the context of other surface measurements and other hypotheses for the spatial distribution of pits on the cells in SP, such as control of the pit distribution due to a thermal gradient across the cells (e.g. White et al., 2017).

2. Methods

2.1 Pit Distribution Determination

We map pits on 7 cells in 80 m/px Long Range Reconnaissance Imager (LORRI; Weaver et al. 2008) imagery using ArcMap 10 (Fig. 1, 2, 3). We select the cells based on complete (or nearly complete) LORRI data coverage. We estimate a 1σ Gaussian error of 1 px (80 m) in the mapped diameter of each pit.

After mapping, we prepare the data for spatial analysis. We divide cells I, II, III, and IV into top, bottom, left, and right quadrants based on their elongated shape and obviously radially asymmetrical pit distributions (Fig. 2, 3). We fit the quadrants separately. In the left and right quadrants we take distance *x* to be the perpendicular distance from a line segment that maps the spreading center. In the top and bottom quadrants, we take *x* to be the distance from the top (or bottom) termination of the line segment mapping the spreading center (Fig. 3). For cells V, VI, and VII we take *x* to be the distance from the estimated central point. We map the central spreading line (or point) based on the approximate bisecting line (or central point) of the contiguous central region of the cell that has low variance at LORRI resolution (e.g. White et al. 2017). These regions correspond to distinctive textures (e.g. Fig. 2). We test the sensitivity to our choice of spreading center by shifting the line (or point) by 10% of the maximum width of each cell (several kilometers) and by rotating the lines by 10 degrees. In all but two cases, the fits to pit radius *r* vs. *x* are affected by <20% (also <2σ). The exceptions are the fit to the left quadrant of cell IV, which varies by up to 40% (2.5σ), and the left quadrant of cell III, which appears to have a complex history and is discussed in more detail in §4.5.

Top and bottom quadrants typically contain many fewer pits than left and right quadrants and the *r* vs. *x* distribution is strongly dependent on the mapped location of the spreading center. Therefore, we choose only to analyze *r* vs. *x* in the left and right quadrants of cells I, II, III, and IV.

We fit a linear, analytic least-squares regression to *r* vs. *x* for each cell (Fig. 4; e.g., Press et al., 1987). We also perform higher-order polynomial fits to the *r* vs. *x* distribution. However, the nonlinear coefficients in these fits are indistinguishable from zero and the constant and linear terms do not differ from the linear fit at the 0.5σ level. Calculating the Bayesian Information Criteria (BIC) for each model—which quantifies the trade-off between model goodness of fit (favored) and complexity (disfavored)—the difference in BIC (ΔBIC) between the linear and quadratic models for each cell ranges from 5.9 to 7.2. This strongly indicates that nonlinear models are not justified by the data (e.g., Kass & Raftery, 1995); higher-order polynomials are even more strongly disfavored. In other words, *r* vs. *x* is linear within error, even though we do not generally expect constant velocity spreading (see §4.2).

2.2 Analytic Sublimation Model

We use the *r* vs. *x* distribution to determine the age vs. *x* distribution (i.e., the surface velocity *v*) by calculating the rate of pit enlargement using a simple analytic model. The model provides a closed-form expression for the total energy absorbed by the walls of a pit under the assumption that the pit is a spherical cap (Ingersoll et al. 1992).

Pit walls receive power from both direct insolation and from scattered sunlight. The extra power absorbed by scattering means that an area subtended by a pit receives more power, as compared to a flat surface, according to (Ingersoll et al., 1992):

(1) $$P_{Pit} = I_0 \left(\frac{1-A}{1-Af}\right)$$

Here P_{Pit} is the power per area absorbed by a flat surface subtended by a pit (including both direct insolation and scattered light), I_0 is the solar insolation (irradiance times the cosine of the incidence angle), and A is the albedo. The factor $f = 1/(1 + D^2/4)$ describes the geometry of the pit (D is the diameter/depth ratio); f = ½ describes a hemisphere and f = 0 describes a flat surface (see Ingersoll et al., 1992; Fig. 5). Eq. 1 assumes Lambert scattering. Thus, if both A and f are nonzero, then P_{Pit} is greater than the power per area absorbed by a flat surface $P_{Flat} = I_0(1 - A)$.

Similarly, the outgoing emitted power per area from a surface subtended by a pit E_{pit} is (Ingersoll et al., 1992):

(2) $$E_{Pit} = \frac{\varepsilon\sigma_B T_{Pit}^4}{1-(1-\varepsilon)f}$$

Here ε is the emissivity, σ_B is the Stefan-Boltzmann constant, and T_{Pit} is the temperature of the pit walls. Notice that if $T_{Pit} = T_{Flat}$ (the temperature of a flat surface) and $\varepsilon = 1$, then E_{Pit} is the same as the emitted power per area from a flat surface $E_{Flat} = \varepsilon\sigma_B T_{Flat}^4$. Thus, when both these conditions are fulfilled, the reradiated thermal energy does not enhance sublimation within a pit relative to a flat surface. The N_2 ice in SP is likely in exchange equilibrium with the atmospheric N_2, implying the surface is isothermal and thus that $T_{Pit} = T_{Flat}$ (e.g. Hansen & Paige 1996; Moore et al. 2016a). Protopapa et al. (2016) report 59 cm grain sizes in SP based Hapke analysis (with unknown error). This grain size implies that $\varepsilon = 1$, according to the model of Stansberry et al. (1996) for β-N_2, the stable phase at the surface of SP (e.g., McKinnon et al., 2016). Therefore, we take $E_{pit} = E_{flat}$, which means that the net outgoing reradiated power per area from an area subtended by a pit equals that of a flat surface.

Based on the analysis above, the net difference in power per area between a flat surface and a flat surface subtended by a pit is the scattered power per unit area P_S, which is (Ingersoll, 1992):

(3) $$P_S = I_0 A f \left(\frac{1-A}{1-Af}\right)$$

An equivalent statement is $P_S = P_{Pit} - P_{Flat}$. We thus take P_S to be the power per unit area available to sublimate the pit walls and cause radial growth of the pits.

Under the assumption that the pit is a spherical cap, every point on the surface receives the same P_S (Ingersoll et al., 1992). Because P_S is comparable to P_0 and Pluto's high obliquity will cause the angle of the sun on the sky to sample a wide region of parameter space, power will be absorbed approximately evenly over the pit walls. Thus, as N_2 ice is lost to sublimation, we assume the pit remains a spherical cap with constant *D*, and determine the growth rate due to sublimation evenly distributed over the surface area of the curved walls of the pit $S_{pit} = \pi r^2(1 + 4/D^2)$.

We use *A* between 0.95 and 0.98, with uniform probability (see Buratti et al., 2017; J. Hofgartner, per. comm.), $I_0 = 0.22$ W m^{-2} (average value over the past 1.3 Myr at 0° latitude (Earle & Binzel, 2015)), N_2 ice density of 1027 kg m^{-3}, and N_2 ice latent heat of 2×10^5 J kg^{-1}. Shadows typically extend 0.5 ± 0.25 of the way across pits, which we take to be a Gaussian distribution accounting for observational uncertainty and actual variation in pit depths. Based on photogrammetry[1], we estimate that pits have depth/diameter ratios of 0.35 ± 0.09 (with Gaussian errors), yielding $f = 0.32^{+0.11}_{-0.10}$. We also impose a prior that pits are shallower than hemispheres (i.e. f ≤ ½) and that pits are deep enough to have shadows, which is a universal feature of all pits we map (e.g. Fig. 1, 2) and implies that f ≥ 0.11 (Fig. 5).

The radiative transfer model is potentially sensitive to *A* because the power per area depends on 1-*A* and *A* is near 1. However, as long as *A* > 0.9, the growth rate we report remains the same within a factor of ~3. Likewise, as long as ε > 0.9, which we expect for grain sizes larger than ~5 cm (see figure 2

[1] Illumination geometry calculated based on ephemeris from Pluto Ephemeris Generator 2.6 (http://pds-rings.seti.org/tools/ephem2_plu.html by Mark Showalter)

of Stansberry et al., 1996), the growth rate we report remains the same within a factor of ~3. We note that, while the global plutonian atmosphere may periodically collapse, a local atmosphere will likely remain over regions covered by large N_2 ice deposits, like Spunik Planitia (Hansen and Paige, 1996). Thus, we expect radiative balance, not vapor diffusion into the atmosphere, will always control sublimation. "Year" refers to terrestrial year throughout this paper.

3. Results

3.1 Pit Distribution and Convection Rates

We map 12,297 pits across all seven cells (Fig. 1, 2, 3). Cells range in area from 150-1050 km^2, with 354-2989 pits per cell and an average of 2.0-2.9 pits per km^2 (Table 1). At LORRI resolution, pits cover between 24%-33% of the surface of the cells (Table 1). The slope of the *r* vs. *x* distribution of pits ranges from 2.1 ± 0.4 × 10^{-3} m m^{-1} to 5.9 ± 0.8 × 10^{-3} m m^{-1}. The intercept of the *r* vs. *x* distribution of pits ranges from 128 ± 3 m to 186 ± 8 m. Table 2 contains the complete list of best-fit parameters.

The analytic sublimation model yields a growth rate of $3.6^{+2.1}_{-0.6} \times 10^{-4}$ m yr^{-1} (Fig. 6). This implies that surface velocities range from $6.2^{+3.8}_{-1.4}$ cm yr^{-1} to $19.9^{+11.7}_{-4.4}$ cm yr^{-1} (Fig. 7). This surface velocity is similar to the results of the McKinnon et al. (2016) convection model, which predicts ~6 cm yr^{-1} convection rates (with a factor of a few uncertainty; W. McKinnon (pers. comm.)), supporting the hypothesis that the cells are the surface expression of convection in the sluggish lid regime. The errors quoted here take into account the uncertainty in *A* and *f*, but do not take into account the possible effects of viscous relaxation of pits, resolution limit of the dataset, or mergers between pits. We discuss these in §4.1, §4.2, and §4.3.

The *r* vs. *x* distributions for all cells except the left quadrant of cell III have slopes that are nonzero at the 3σ level (Table 2). We infer that a complex geologic history, including unstable convective interaction between cells I, II, and III, causes the left quadrant of cell III to be different and discuss this further in §4.5.

4. Discussion

4.1 Cell Surface Rheology

The main components of SP are likely N_2 and CH_4 ice (Protopapa et al., 2017). However, the rheology of N_2 and CH_4 ice under conditions relevant to the surface of Pluto is uncertain (see, e.g. Moore et al., 2016b). For CH_4, Moore et al. (2016b) find a nine order of magnitude discrepancy in viscosity between extrapolated laboratory measurements from Yamashita et al. (2010) and theoretical predictions from Eluszkiewicz and Stevenson (1991). Moore et al. (2016) suggest that the use of laboratory-annealed CH_4 ice in the Yamashita et al. (2010) experiments may lead to the divergent results. Similarly, we calculate a nine order of magnitude difference in N_2 viscosity between extrapolated laboratory measurements from Yamashita et al. (2010) and theoretical predictions from Eluszkiewicz and Stevenson (1991).

4.1.1 Laboratory and Theoretical Predictions for N_2 Rheology at Plutonian Surface Conditions

Yamashita et al. (2010) perform compression experiments on N_2 ice at 45 K and 56 K and stresses between ~0.1-1 MPa. Pluto's surface temperature is 37 K (Gladstone et al., 2016; Stern et al., 2015) and the stress at the bottom of a pit Σ is ~7×10^{-2} MPa (from $\Sigma = \rho g h$; ρ is the density of N_2 ice,

g is the plutonian surface gravity (0.617 m s^{-2}), and we set *h* = 100 m for definitiveness). We extrapolate from the stresses in the Yamashita et al. (2010) experiment to those in a pit bottom using the empirical relation for scaling the N_2 viscosity η reported by Yamashita et al. (2010). To extrapolate the experimental results to the plutonian surface temperature we use (Weertman, 1970):

(4) $$\eta_1 = \eta_0 \, exp\left[-a\left[\frac{T_m}{T_0} - \frac{T_m}{T_1}\right]\right]$$

Here T_0 is the temperature at which the viscosity is known, T_1 is the temperature at which the viscosity is desired. T_m= 63.15 K (Eluszkiewicz & Stevenson, 1991) is the melting temperature of N_2 ice, and *a* is an empirical constant (estimated here to be ~5 by applying Eq. 4 to the viscosities measured by Yamashita et al. (2010) at 45 K and 56 K). This yields an expected viscosity of approximately 10^{10} Pa s.

A theoretical derivation of the rheology of N_2 in the diffusion limit (Eluzkiewicz and Stevenson, 1991) indicates that the viscosity may be much higher. Following the suggestion of Eluzkiewicz and Stevenson (1991), we use their Figure 1 to scale derived CH_4 rheologic properties to N_2 rheologic properties. This exercise implies strain rates of ~10^{-15} s^{-1} for applied stresses at pit bottoms (~0.1 MPa) for an N_2 ice shear stress of 20 GPa (Eluzkiewicz and Stevenson, 1991), implying a viscosity of ~10^{19} Pa s. We note (i) that the theoretical prediction is based on sparse data, extrapolations over many orders of magnitude, and reliance on the similarity between CH_4 and N_2 and (ii) we have extrapolated beyond the pressure and temperature ranges measured in the Yamashita et al. (2010) experiment. It is clear that rheology of N_2 ice at plutonian surface conditions is not well known.

4.1.2 Estimate of Surface Viscosity Based upon the Presence of Pits

We may estimate the viscosity-dependent relaxation timescale for pits (i.e., the characteristic timescale for pits to flatten due to viscous flow). The relaxation timescale appropriate to pits embedded in a homogeneous viscous layer of thickness *d* overlying an inviscid, vigorously convecting layer is (Solomon et al., 1982):

(5) $$t_r = \frac{2\eta k}{\rho g}\left[\frac{e^{2kd}+e^{-2kd}-4(kd)^2-2}{e^{2kd}-e^{-2kd}+4kd}\right]$$

Here *k* is the wavenumber (2π divided by the pit diameter (300 m, for definitiveness)), and t_r is the time for topography to relax by a factor of 1/e; t_r is insensitive to *d* when *d* exceeds the pit depth. Note that we could also choose a prescription in which the viscosity increases exponentially with depth (e.g. due to increasing temperature with depth). Under this prescription, the long wavelength limit approaches Eq. 5 and the short wavelength limit approaches relaxation in a uniform viscosity material, $t_r = 2\eta k/\rho g$ (see equations 8.4.10-8.4.15 of Melosh, 1989); this does not change our conclusions.

Using η = 10^{10} Pa s (based upon Yamashita et al. (2010)) yields a t_r of ~7 days. Using η = 10^{19} Pa s (based upon Eluzkiewicz and Stevenson (1991)) yields a t_r of ~2 × 10^7 yr. Based on the $3.6^{+2.1}_{-0.6} \times 10^{-4}$ m yr^{-1} radial growth rate of pits that we calculate, the observed pits with radii of a few hundred meters should take on the order of 10^5 yr to form. This implies that relaxation timescales should be at least this large; otherwise, the pits would relax away before reaching their observed size. Relaxation timescales of >10^5 yr imply a minimum viscosity of at least ~10^{16} – 10^{17} Pa s.

We therefore conclude that the observation of pits in SP is consistent with the theoretical prediction of N_2 ice viscosity from Eluzkiewicz and Stevenson (1991), but inconsistent with the values reported by Yamashita et al. (2010) (also noted by Moore et al., 2016b). There are several potential reasons for the inconsistency. First, the laboratory-annealed N_2 ice may not be representative of the ice in SP (Moore et al., 2016b). Second, the mixture of different ices (N_2, CH_4, and others) present at the

surface of SP may have an increased viscosity compared to the single phases (Moore et al., 2016b). Third, power-law flow—as was observed for N_2 ice by Yamashita et al. (2010)—is typically strongly grain-size dependent (e.g. Durham et al., 2010), and scales as the inverse square ("Nabarro-Herring creep") or inverse cube ("Coble creep") of the grain size. While Yamashita et al. (2010) do not report grain sizes in their N_2 ice experiments, they report that the ice was polycrystalline and the experimental chamber was 10 x 15 mm, implying that the grain sizes were several mm or smaller. Eluszkiewicz & Stevenson (1991) derive rheologies based on 0.1 mm grain sizes. Grain sizes for the surface of SP are reported to be 59 cm (Protopappa et al., 2017) based on Hapke modeling. While there is uncertainty associated with the Hapke modeling, grains may realistically reach this scale based upon modeling by Zent et al. (1989), which shows that N_2 ice grains on Triton, under conditions similar to Pluto, should sinter to meter-scale grains within ~100 yr. We note, though, that nonvolatile impurities, such as tholins, could arrest grain growth (e.g. Barr and Milkovich, 2008). If the grain sizes reach tens of centimeters or larger, the viscosity reported by Yamashita et al. (2010) could scale up by six to nine orders of magnitude, which would be consistent with the observed pits in SP.

Finally, we note that, while grains can coarsen due to annealing, grain size can also decrease due to dynamic recrystallization under high stress (e.g., Durham et al., 2010), such as might occur in underlying convecting ice. Therefore, the grains sizes and viscosities relevant to pit relaxation need not be the same as those relevant to convection (e.g. Umurhan et al., 2017). Clearly, there is much to learn about the rheologic properties of these ices.

4.1.3 Radial Growth Dominated by Sublimation

We argue that viscous relaxation will not significantly affect the radial growth rate of the pits, as follows. We observe pits (they have not relaxed away), and so expect that the sublimation of the pit

floor is at least in equilibrium with relaxation at the bottom of the pit. Long-wavelength relaxation (e.g. uplift of the pit floor) will proceed on much shorter timescales than short-wavelength relaxation (e.g. flow of pit walls) (e.g., Melosh, 1989; Moore et al., 2016b). Therefore, the uplift rate of the pit floor will exceed the flow rate of the walls near the rim, and sublimation rates will dominate viscous flow in setting the radial growth rate. Thus, the dominant topographic influence of viscous relaxation on large (~100 m radius) pits will be to set the depth of the pits, similarly to the way craters on icy satellites relax in depth while preserving their diameters (e.g. Parmentier and Head, 1981). We conclude, then, that viscous relaxation does not strongly affect our measurement of the pit radius distribution, except inasmuch as viscous control of pit depths may influence growth rates of pits through the depth/diameter ratio (§2.2, Eq. 3, Figs. 5 & 6).

4.2 Pit Distribution Linearity and Nonzero Intercept

4.2.1 Expected Surface Velocity Profile and Pit Distribution

An upwelling plume of finite width should have a distally accelerating surface velocity gradient over the plume, with horizontal velocities near stagnation at the center of the plume (Fig. 8; McKinnon et al., 2016). If the surface velocity reaches large enough values, such that lateral transport of pits significantly outpaces the formation of new pits, then, in the accelerating region, pit density should decrease because the flux of pits carried into a region will be lower than the flux out. Thus, in the central region of the cell, we expect a stagnant, densely pitted region surrounded by a less densely pitted, accelerating region.

Distal to the upwelling region, we expect two end-member possibilities. If the cell is axially symmetric, the velocity will asymptotically decrease (due to continuity) at a rate inversely proportional

to the distance from the cell center (Fig. 8; McKinnon et al., 2016). If the cell is bilaterally symmetric, the velocity will remain near a constant value (also due to continuity) (Fig. 8). In both cases, we expect an evenly dense distribution of pitting because the inward and outward flux of surface material is constant across this region.

Therefore, distal to the central upwelling region, we expect the bilaterally symmetric cells (I, II, III, and IV) to have a linear increase in pit size due to a transport at a constant surface velocity. We expect the axially symmetric cells (V, VI) to have a quadratic increase in pit size due to transport at a velocity that is decreasing at a rate inversely proportional to the distance from the cell center. Cell VII is neither radially nor axially symmetric but, due to its elongated nature, we expect the surface velocity profile to more closely resemble the bilaterally symmetric, constant velocity case. We also expect that the scatter in pit sizes, coupled with effects from viewing the cells at finite resolution will affect our determination of the slope and intercept of all of the pit distributions.

4.2.2 Qualitative Resolution Effects

Resolution limits will conceal the small-radius population of pits. This means that only the largest pits on the younger, more central surfaces will be visible and these surfaces will appear less densely pitted. We attribute the nonzero intercept to this effect and interpret that the intercept probes the maximum timescale over which pits reside near the stagnant cell center (see §4.4). The large scatter in pit radii may be partially due to variable duration spent near the stagnant region of the cell, because residence time (and thus growth time) near the cell center will vary strongly as a function of distance from the center of the cell because the surface is accelerating (Fig. 8C and 8D).

As a parcel of the cell surface moves away from the cell center and ages, the pits in that parcel grow larger and become visible at LORRI resolution. This causes the density of observable pits to

increase with distance from the cell center, which is consistent with observation (Fig. 3 & 9). This effect also artificially decreases the observable pit size distribution on older surfaces relative to younger surfaces, which will decrease the best-fit slope and increase the intercept (Fig. 8). The increased observability of the small-radius population with age will also dilute the signal of surface velocity deceleration, if present. We propose that this dilution, compounded with the large measurement errors relative to the absolute pit sizes, means that the second order features (acceleration) in the velocity curve expected in the axially symmetric cells (V and VI) could not be resolved with the current data. Note that cells V and VI are also significantly smaller and have proportionally fewer pits relative to other cells (Table 1), further reducing the ability to fit higher order features in their distribution (Fig. 8H).

4.2.3 Quantitative Resolution Effects

Pits with radii of 80 m (i.e., distinguishable at the 2σ level, for 1 px errors on pit diameters) should take $2.2^{+0.5}_{-0.8} \times 10^5$ yr to grow at our calculated radial growth rate of $3.6^{+2.1}_{-0.6} \times 10^{-4}$ m yr^{-1}. This means that the resolvable pit distribution within ~10 km of cell centers should be dominated by pits forming in the stagnant, central region of the cell because pits forming on distal, more rapidly moving regions (e.g. >5 cm yr^{-1}; cf. Table 2) will travel ~10 km before growing large enough to be resolved. In other words, we expect that most pits forming in the stagnant region will have grown large enough to be visible at LORRI resolution at ~10 km distance from the cell center and most pits forming distal to the stagnant center will not yet be visible. Thus, we expect that the *real* pitting density in the stagnant region should be approximately the same as the *observed* pitting density at a distance of ~10 km from the cell center. We use this expectation to estimate the effect of resolution on the intercept and the slope by assuming that only resolution effects cause decreased pitting density near the center of the cell.

Note that this will overestimate the effects of resolution because the region of accelerating surface velocity should have intrinsically fewer pits (§4.2.1).

To perform this estimate, we divide the pits into 1 km-wide bins and find the bin with the highest pitting density, which is typically ~10 km from the center, in a region where the pitting density plateaus (e.g. Fig. 9A). We then inject an artificial population of small pits such that the pitting density is the same as the maximum pitting density in each bin interior to the bin with the maximum pitting density (Fig. 9C). We respect the geometry of the cells when calculating the pits per area, i.e. bins in the bilaterally symmetric cells are strips, whereas the bins in the radially symmetric cells are annuli. We assign 40 m radii to the injected pits to simulate the mean value of a population of pits that is equally dispersed between a radius of zero (just formed) and a radius of 80 m (just below resolution at the 2σ level). We summarize the effect of artificially injecting pits below resolution in Table 3.

As expected, injecting small-radius pits causes the intercept to decrease and the slope to increase, leading to a decrease in the inferred average velocity by a factor of ~2-4. Because we expect pits to be below resolution, we expect the velocities quoted in Table 3 to be more accurate than the velocities quoted without taking resolution effects into account (Table 2; Fig. 8G). However, this injection method overestimates the effect of resolution because the region of accelerating surface velocity should have intrinsically fewer pits (§4.2.1). Thus, our preferred interpretation is that the velocities of cells lie in the range between the best-fit values reported in Tables 2 and 3. Notably, these fits show that the axially symmetric cells (V and VI) have lower average velocities than the bilaterally symmetric cells (I, II, III, IV) and the distorted cell (VII). We speculate that this may be a signal of the averaged effect of the decreasing velocity gradient with distance from the cell center in radially symmetric cells, even though the velocity gradient itself cannot be resolved.

Finally, we note that the density of pits is low not only near the centers of cells, but also near the edges (Fig. 9; see also Moore et al., 2016b; White et al., 2017). The lower pitting density near the edges cannot be explained by resolution effects; we speculate on the cause of this low density in §4.6.

4.3 Mergers between Pits

We can estimate how mergers between pits affect the fit, under the assumption that pits with radii separated by a distance *Δx* less than one pixel (80 m) are erroneously mapped as a single pit. The average pit density across most cells is 2-3 pits per km^2, with the most densely packed locations reaching ~4 pits per km^2. For a small number of pits *n* we can approximate the probability of two pits overlapping as being independent and thus estimate probability that any particular mapped pit is actually two merged pits as $\sum_{n=1}^{n=4} n\pi(\Delta x)^2/1\ \mathrm{km}^2 = 12\%$. Thus, we expect that merging between large pits (visible at LORRI resolution) will minimally affect our fit. However, we cannot probe the smaller-radius distribution of pits, and mergers between small pits forming on the relatively small stagnant region may act to increase the pit radii there more rapidly than sublimation alone, acting to increase the intercept in the fit to the *r* vs. *x* distribution.

4.4 Cell Surface Ages

The directly measured pit distribution (§3.1, Table 2) and the distribution after taking into account likely bias from resolution (§4.2.3, Table 3) allow us to estimate surface ages of the cells. The intercepts of the *r* vs. *x* fits using the directly measured distribution range from 128-186 m (Table 2), implying that pits spend $3.5 - 5.2 \times 10^5$ yr near the stagnant cell centers, based on a radial growth rate of 3.6×10^{-4} m yr^{-1}. The resolution-adjusted fit (Table 3) yields intercepts of 71-128 m, implying

that pits spend $2.0 - 3.5 \times 10^5$ yr near cell centers. The convection length divided by the convection rate yields the characteristic convection timescales. For the directly measured distribution, this yields timescales of $7.3 \times 10^4 - 3.5 \times 10^5$ yr (Table 2). For the resolution-adjusted fit, this yields timescales of $3.0 - 5.3 \times 10^5$ yr (Table 3). Therefore, our preferred interpretation is that surfaces near cell edges reach ages of $4.2 - 8.9 \times 10^5$ yr, i.e., the sum of the time spent near stagnation and of the time spent traveling across the cell. These ages refine the age constraints on the surface of SP of < 10 My from the lack of observed impact craters (Moore et al., 2016a) and of ~5×10^5 years from the convection model of McKinnon et al. (2016), and provide error bars on the age estimate.

4.5 Evidence for Convection Instability

All *r* vs. *x* distributions have nonzero slopes in the direction perpendicular to the mapped spreading center at the 3σ level, except for the left quadrant of cell III (Table 2). However, the left quadrant of cell III has a non-zero slope at the 3σ level in the direction *parallel* to the mapped spreading center of cell III, with bilateral symmetry (Fig. 10). Only the right quadrant of cell I also has this property (Fig. 11). The right quadrant of cell I and the left quadrant of cell III border cell II, which has a convection pattern perpendicular to those of cell I and III (Fig. 2, 3). Thus, there is a pattern on cell I and cell III with increasing pit radius with distance from the spreading center of cell II, which we interpret to indicate interaction between the convection underlying these three cells.

The bounding trough between cell I and cell II is also disrupted approximately symmetrically about the inferred spreading center of cell II (Fig. 2). We interpret this as evidence that convection under cell II has been migrating laterally from east to west and that new upwelling material has covered an older convective boundary between these cells. Between cell II and cell III, the intact trough (Fig. 2) may correspond to the development of a downwelling limb after the convection pattern under cell II

migrated west. We also note that the lateral distance from the spreading center to the edge of the cell is greater in the direction away from cell II, for both cell I and cell III (i.e. cell I extends farther west and cell II extends farther east). We interpret this asymmetry to be the result of the convection under cell II interacting with cell I and III and causing transport to be more efficient away from cell II. Finally, we interpret these observations as evidence for instability in the convective overturn on timescales comparable to the age of the cells, as predicted by modeling by Umurhan et al. (2017).

4.6 Speculation about Sparse Pitting Near Cell Edges

Both the number of pits per area and the fraction of surface area covered by pits decreases toward cell edges (Fig. 9), and some pits near cell edges appear shallower (Fig. 2). Mergers between pits cannot account for this observation, but the decay of formerly deeper and denser pitting can (Moore et al., 2016b). The convection timescales of a few 10^5 yr are a significant fraction of Pluto's ~3 Myr obliquity-driven climate cycle (Dobrovolskis and Harris, 1983; Earle and Binzel, 2015). In particular, modeling by Stern et al. (2017) suggests that the average annual atmospheric pressure has been waning from a much higher value that peaked ~9×10^5 yr ago. Deposition of N_2 onto the surface as the atmosphere waned would be thicker on older surfaces, such as the periphery of cells. We speculate that there may be a compositional difference between an atmospherically deposited layer of N_2 ice and underlying upwelled N_2 ice, which will be well-mixed with impurities from other ices, like CH_4 (e.g. McKinnon et al., 2016; Protopapa et al., 2017). Because solid CH_4 and N_2 do not appreciably diffuse into each other under plutonian surface conditions, even over the age of the solar system (Eluszkiewicz and Stevenson, 1991), these two layers would remain chemically distinct. We further speculate that such a chemical difference may lead to a rheologic difference, allowing a potentially purer-N_2 atmospheric deposit blanketing the surface to relax faster than the underlying ice, particularly if chemical impurities

are important in increasing the viscosity of the ice (Moore et al., 2016b). Clearly, this hypothesis requires substantial testing, but we present it here because there are currently no other published hypotheses for the sparse and occasionally shallow pitting near cell edges (see Moore et al., 2016b).

4.7 Comparison to Other Proposed Explanations for the Observed Pit Distribution

White et al. (2017) discuss an alternative hypothesis for the apparent smoothness of cell centers. They propose that high subsurface heat flux near cell centers leads to lower ice viscosity and the erasure of pits via relaxation, while lower heat flux near cell edges leads to a higher viscosity that is capable of supporting pit topography. They also suggest that the formation and maintenance of pits on the cells probably occurs on much shorter timescales than the convective flow of N_2 in the sluggish lid regime. However, we calculate sublimation rates indicating that pits grow to radii of a few hundred meters on timescales comparable to the timescales of convective overturn (§4.4, McKinnon et al., 2016). We also observe pitting down to the limits of resolution, even in the centers of cells, where the heat flux is highest (e.g. figure 4 of McKinnon et al., 2016). In particular, we often observe a densely pitted central region surrounded by a more sparsely pitted region, further encircled by a densely pitted outer region (e.g. Fig 1B, 2). We interpret this pattern to be consistent with pits forming on a stagnant region, moving through a region of accelerating surface velocity, and then entering into a region of equilibrium flux of surface material (§4.2.1). We interpret the observation of a densely pitted central region surrounded by a less densely pitted region to be inconsistent with surface smoothness controlled by viscous relaxation alone, in which case the most central region should be the smoothest because the heat flux should be highest through the center. We therefore infer that viscous relaxation is not completely erasing pits on the timescale of convective overturn. Nevertheless, the viscosity of N_2 ice remains poorly constrained, and viscous relaxation may be in equilibrium with sublimation at the bottoms of pits, thereby setting the depth of pits (see §4.1.3).

5. Conclusion

We map the distribution of sublimation pits on the surface of seven convection cells in Sputnik Planitia, Pluto. We find that a linear model with a nonzero intercept best fits the size distribution of pits, which we interpret as being consistent with lateral transport of surface material on a cell with a nearly stagnant center under with a finite resolution in which pits are typically only a few pixels wide. We assess and account for the effect of resolution, which causes an overestimation of the intercept and underestimation of the slope of the linear fit. Using the size distribution of pits, we estimate that average convection velocities across the cells are approximately 10 cm yr^{-1}. This implies that the cell edges reach ages of approximately $4.2 - 8.9 \times 10^5$ yr. We argue that sublimation is the process that primarily sets the radius of the pits because viscous relaxation acts preferentially on long wavelengths (i.e. determining pit depth) as compared to short wavelength (i.e. pit rims) and the pits have not relaxed away. We also contrast our hypothesis that the pitting pattern on cells indicates cell surface velocities (due to transportation of pits growing by sublimation) against the hypothesis that the pitting pattern results from a thermal gradient inducing a viscosity gradient across the cells. We prefer the hypothesis that surface motion of the cell sets the pitting distribution because (i) the sublimation rates we calculate indicate that the production of ~100 m-scale pits takes place on the same timescale as convection and (ii) the presence of dense pitting surrounded by a region of sparser pitting at the centers of some cells is inconsistent with viscous relaxation governed by a monotonic temperature gradient. However, we also note that N_2 ice viscosity is poorly known, with theory and experiment diverging by many orders of magnitude when extrapolated to the conditions relevant to pits in Sputnik Planitia. Finally, correlation between the pitting distributions of three adjacent cells (I, II, and III), along with the disruption of the

bounding trough between cells I and II, indicates that the underlying convection cells interact and are unstable on timescales comparable to the age of the cells.

Acknowledgements

We thank Heather Knutson for insightful conversations on statistical analysis and Dave Stevenson for illuminating discussions about ice rheology. We also appreciate helpful discussions with Orkan Umurhan and Bill McKinnon. Input from Francis Nimmo and two anonymous reviewers improved the quality of this paper. We are grateful for funding from NESSF grant #16-PLANET16F-0071.

Figure Captions

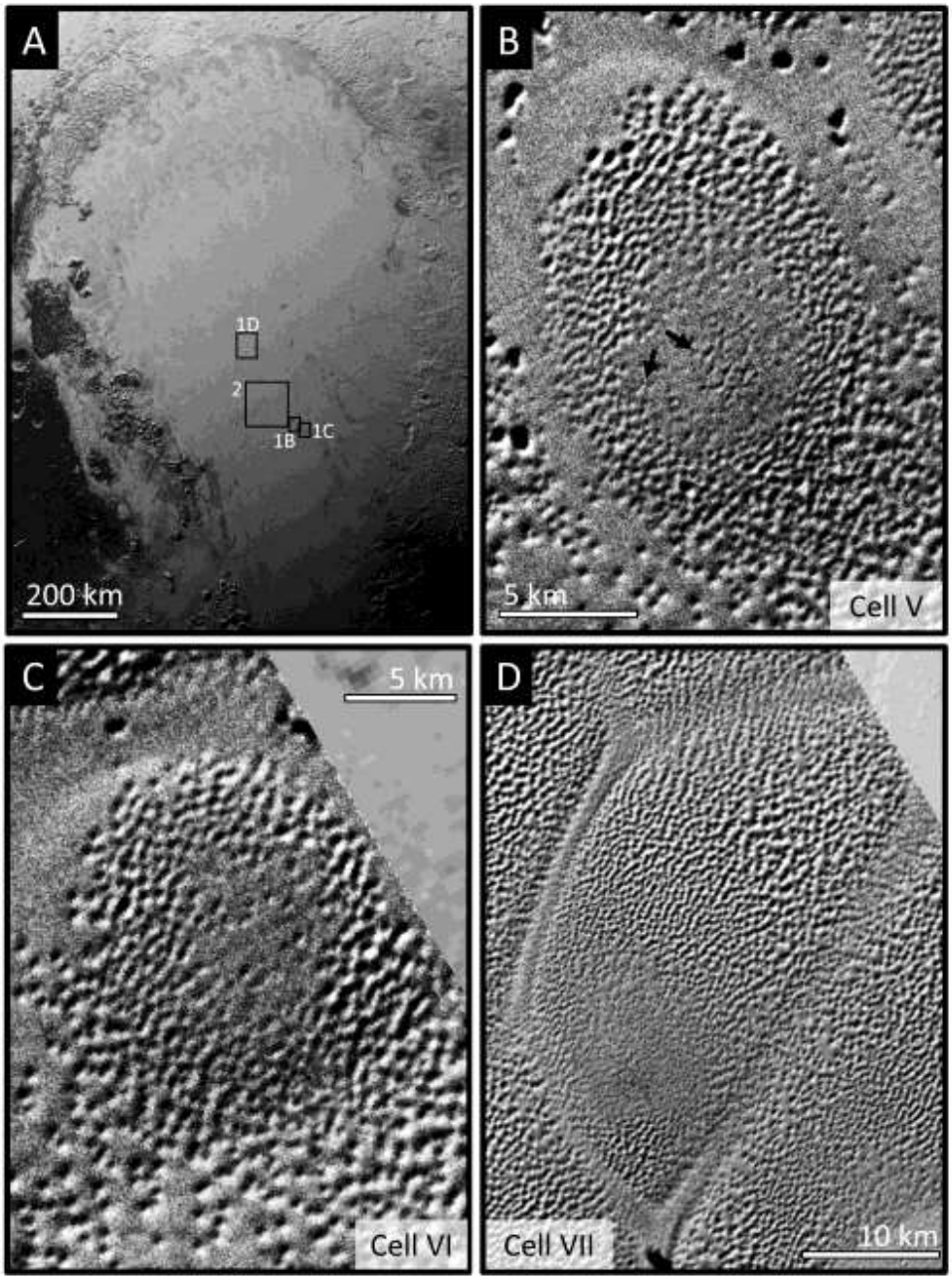

Figure 1. A. Sputnik Planitia with context for Fig. 1B-D, and 2 (black boxes). **B.** Zoom of cell V. Note dense pitting in center, surrounded by region of sparser pitting. Arrows denote edges of sparsely pitted region. Zooms of **C.** cell VI and **D.** cell VII. A. Multispectral Visible Imaging Camera (MVIC) image mp2_0299179552. B-C LORRI images lor_0299179724 and D. lor_0299179715 (B-D contrast enhanced).

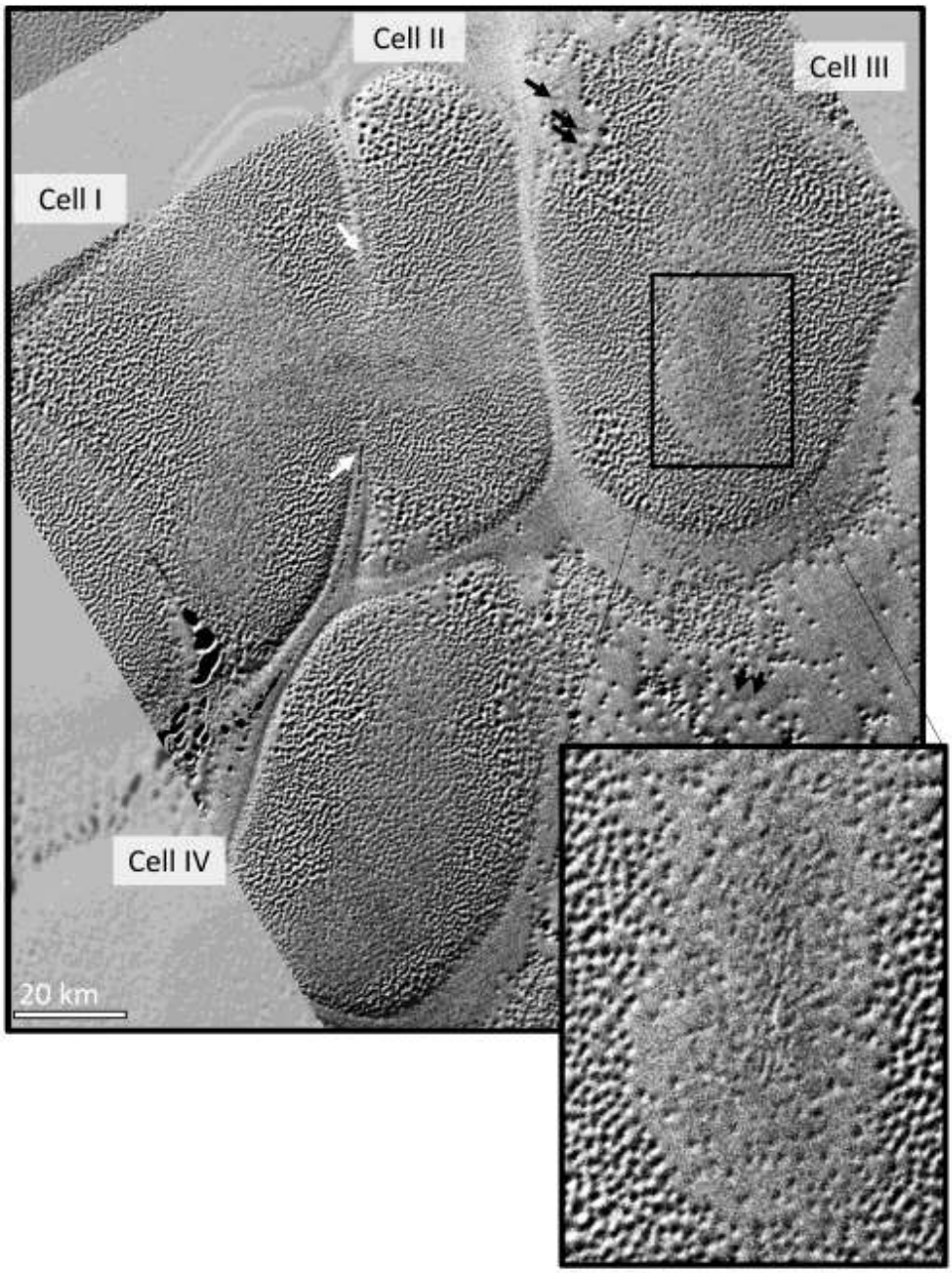

Figure 2. Cells I-IV. Note the zoom in on the central texture of cell III. Black arrows indicate shallow pits. White arrows indicate where the boundary between cell I and II is disrupted. LORRI images lor_0299179718 and lor_0299179724 on MVIC background.

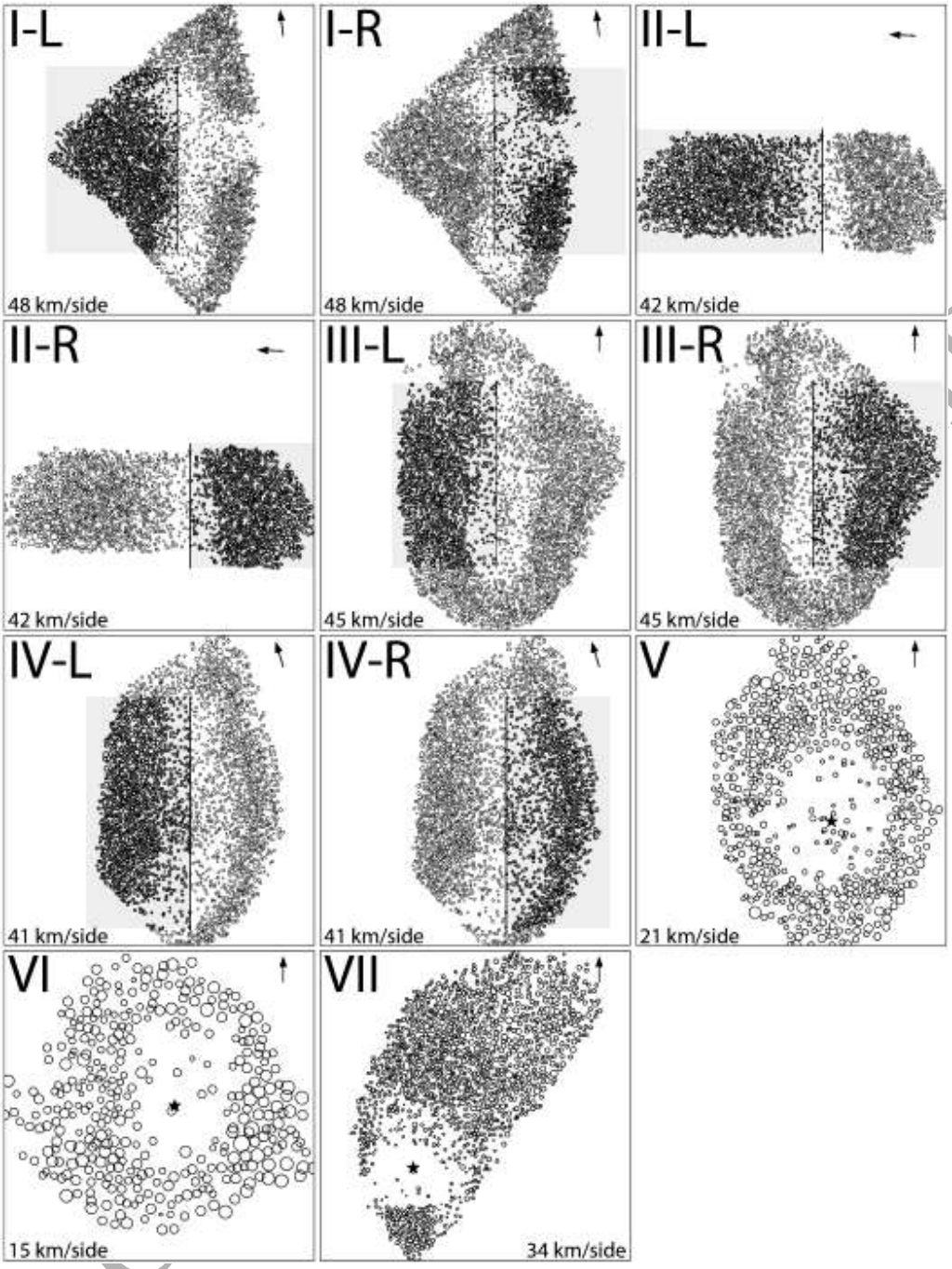

Figure 3. Mapped pits on all cells. Circles in the grayed region are the pits used for fits in Fig. 4 & 7. "L" and "R" designations correspond to "Left" and "Right". Arrows point north. Vertical lines/stars denote spreading center used for the fits in figures 4 and 7. Note map of cell II is rotated ~270 degrees.

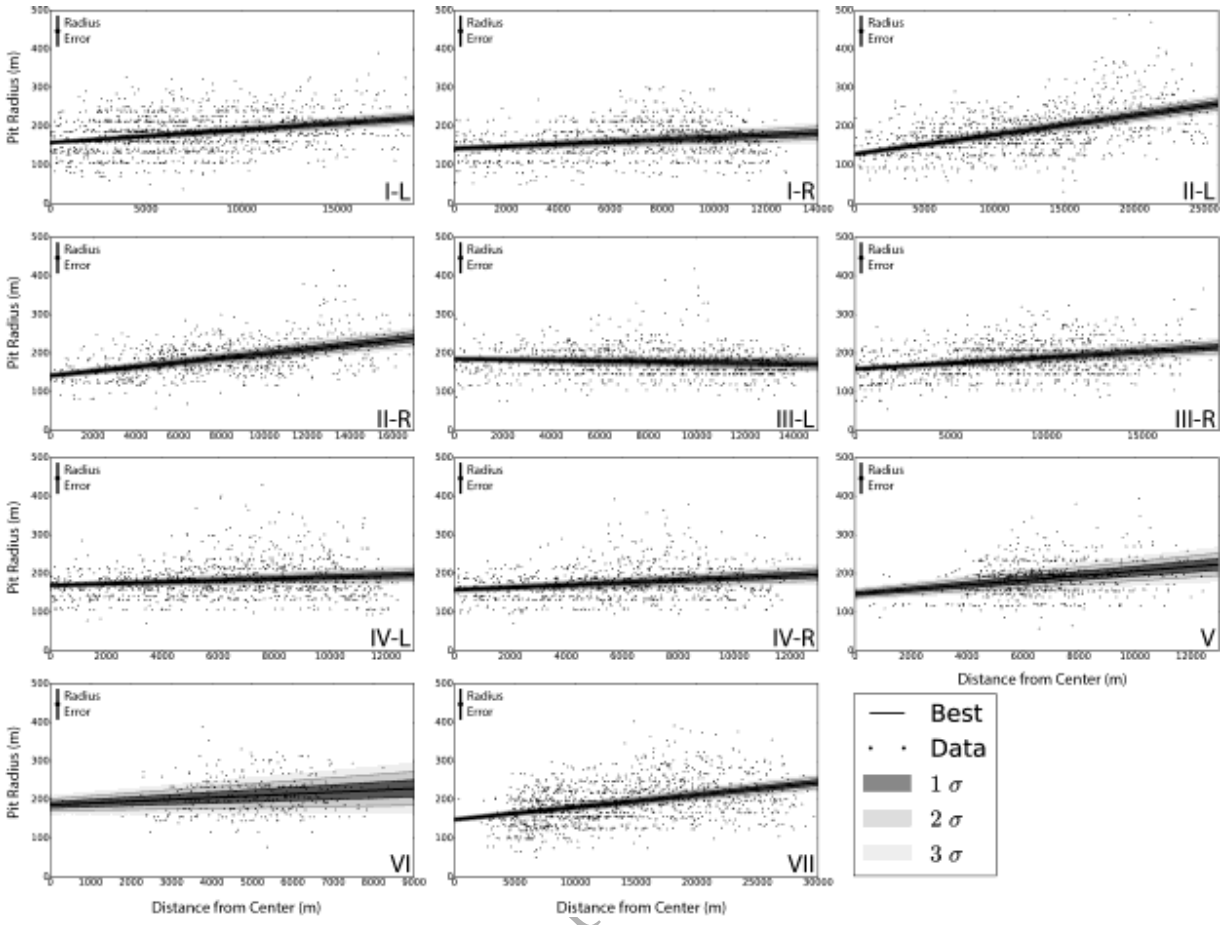

Figure 4. Pit radii as a function of distance from the spreading center, with best fit and 1σ, 2σ, and 3σ uncertainty.

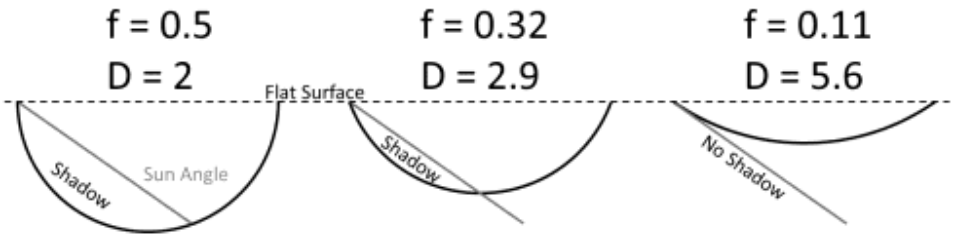

Figure 5. Geometrically accurate depiction of pits with diameter/depth ratios *D* of 2 (hemisphere), 2.9, and 5.6. The corresponding value of *f* is also given. The sun angle and shadowing indicated is faithful to the illumination in Figs. 1 and 2. Pits with these values of *D* receive P_S of 1.1, 0.8, and 0.3 mW/m^2 of scattered power, respectively.

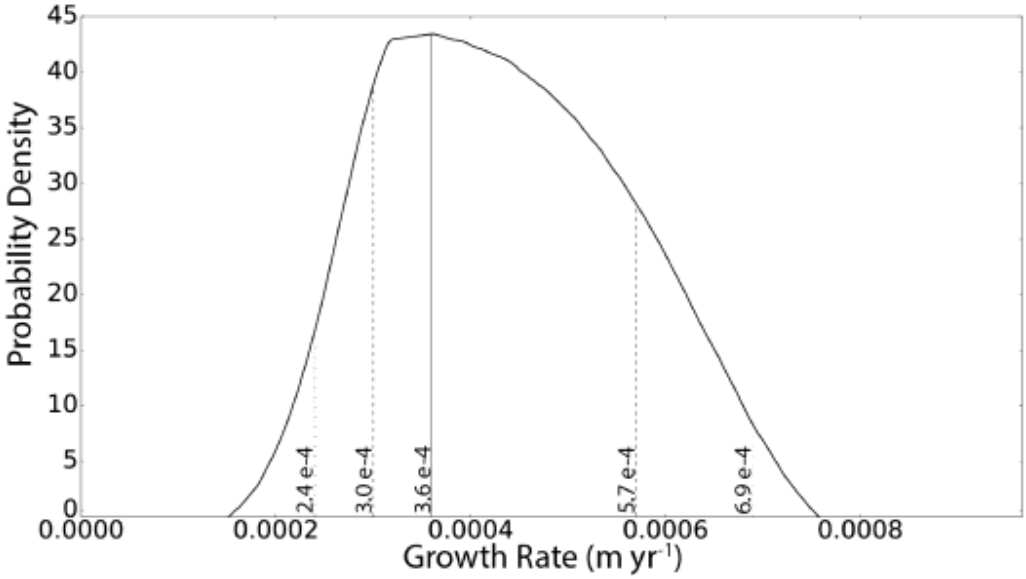

Figure 6. The probability density function of the pit growth rate, with most likely rate (solid), 1σ (dash), and 2σ (dash-dot) uncertainties indicated.

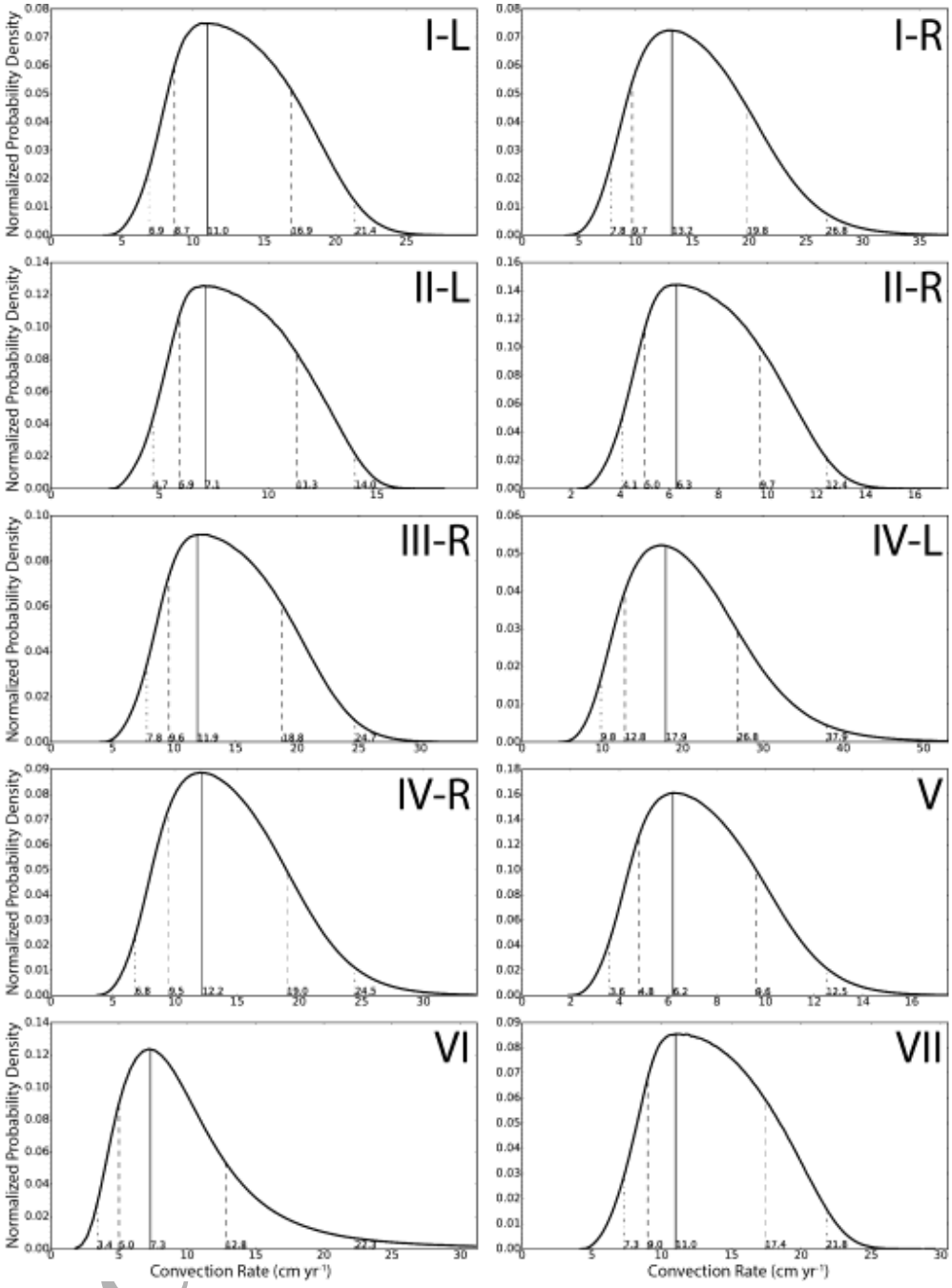

Figure 7. The probability density function of the surface velocity for each cell, with most likely rate (solid), 1σ (dash), and 2σ (dash-dot) uncertainties indicated. Cell III-L has not been included here (see Fig. 10, Table 2).

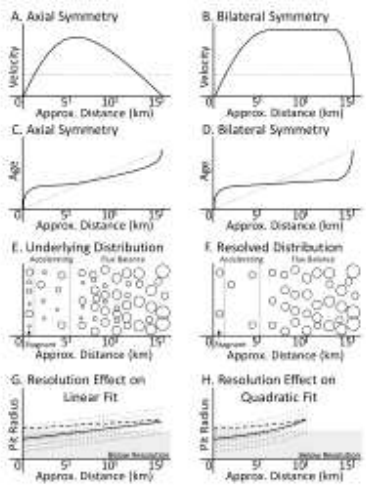

Figure 8. A. Schematic surface velocity profile (thick black) for an axially symmetric cell adapted from figure 4 of McKinnon et al. (2016). Dashed line of constant velocity added for reference. **B.** Schematic surface velocity profile for a bilaterally symmetric cell. The sharp drop off indicates the termination of the cell. **C.** Schematic age vs. distance plot based on the velocity profile in A. **D.** Schematic age vs. distance plot based on B. Note that the slopes in C and D are inversely proportional to velocity and so the age (i.e. residence time) gradient near the cell center is steep. **E.** Schematic depiction of the underlying pit distribution. Note that the accelerating region has a lower density of pits than both the stagnant region and the region where the flux of pits per unit area is constant. **F.** Schematic depiction of pit distribution when viewed at finite resolution. **G.** Schematic representation of the effect of finite resolution to decrease the inferred slope and increase the inferred intercept (dashed line) compared to that of the true distribution (solid line). The gray dots represent a pit radius distribution with high scatter. Gray box indicates region below resolution. **H.** Same as G, but for a quadratic distribution. Note the curvature in the dashed line is reduced compared to the curvature in the solid line. The fit truncates to indicate that the axially symmetric cells have smaller lateral extent, further complicating the fit.

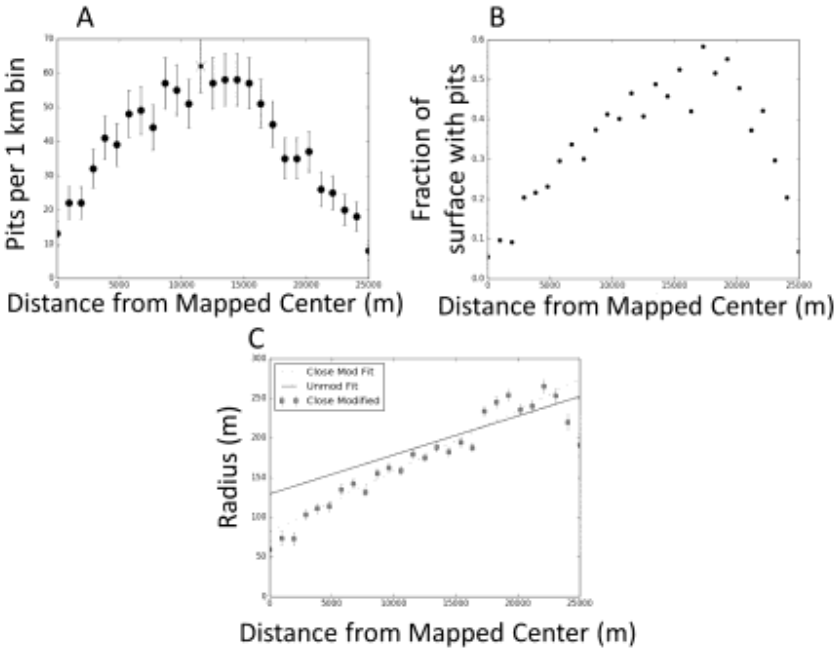

Figure 9. A. The number of pits *N* per each kilometer bin in cell II. The "x" indicates the bin with the largest number of pits per bin. Poisson $\sqrt{N}$ error bars are given. **B.** The fractional area covered by pits in 1 km bins. Note the decrease beyond ~20 km. **C.** Fit to the binned data (dash-dot) after scaling the radii (squares) of the bins interior to bin with the largest number of pits in order to account for pits hidden by resolution. The scaling is described in §4.2.3. Solid line is the fit to the data before accounting for resolution (cf. Fig. 4), for comparison. Poisson $\sqrt{N}$ error bars based on the number of pits in the data before accounting for resolution.

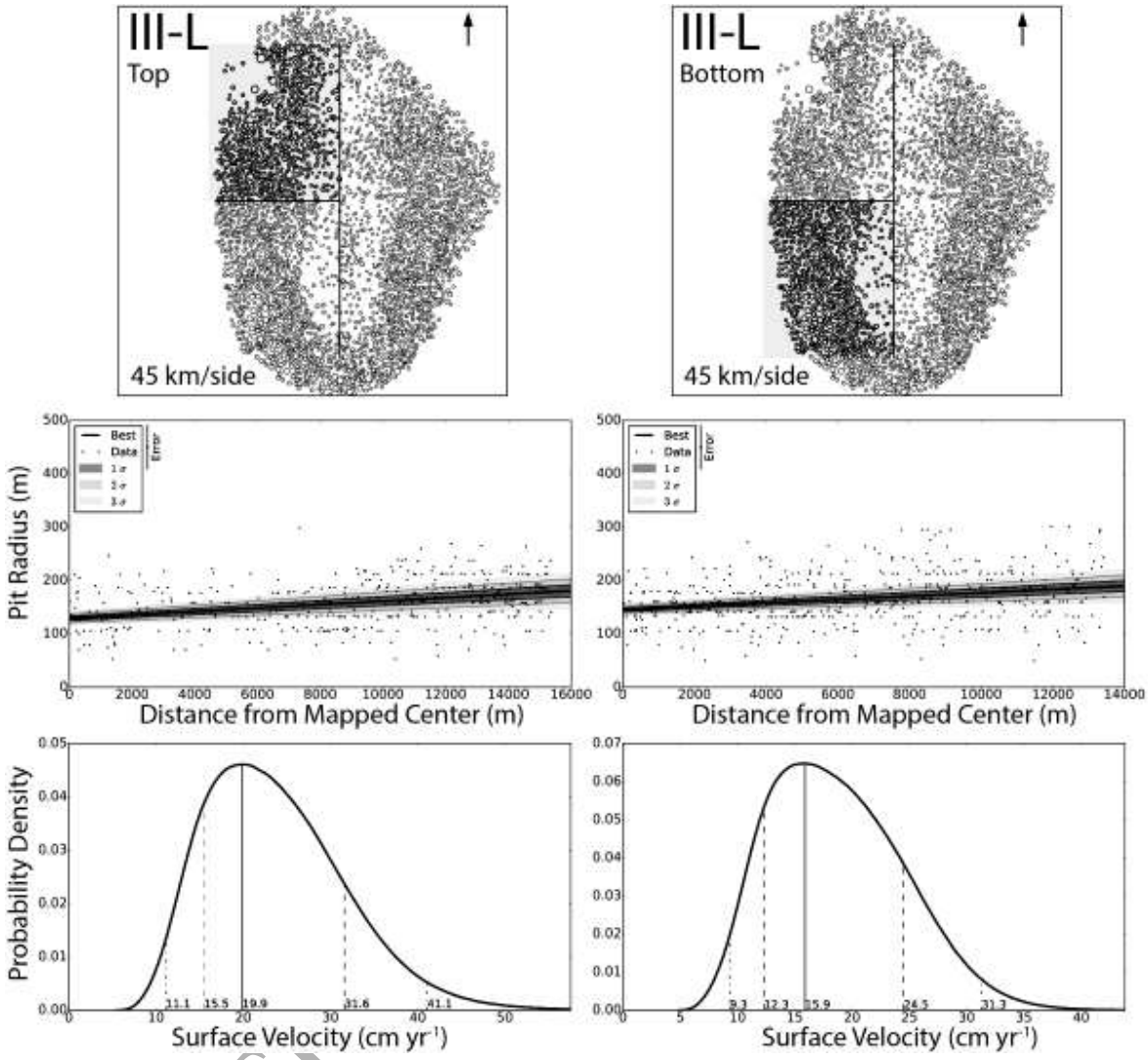

Figure 10. Fits to the upper and lower halves of the left side of cell III, in the same style as Figs. 3, 4, and 7.

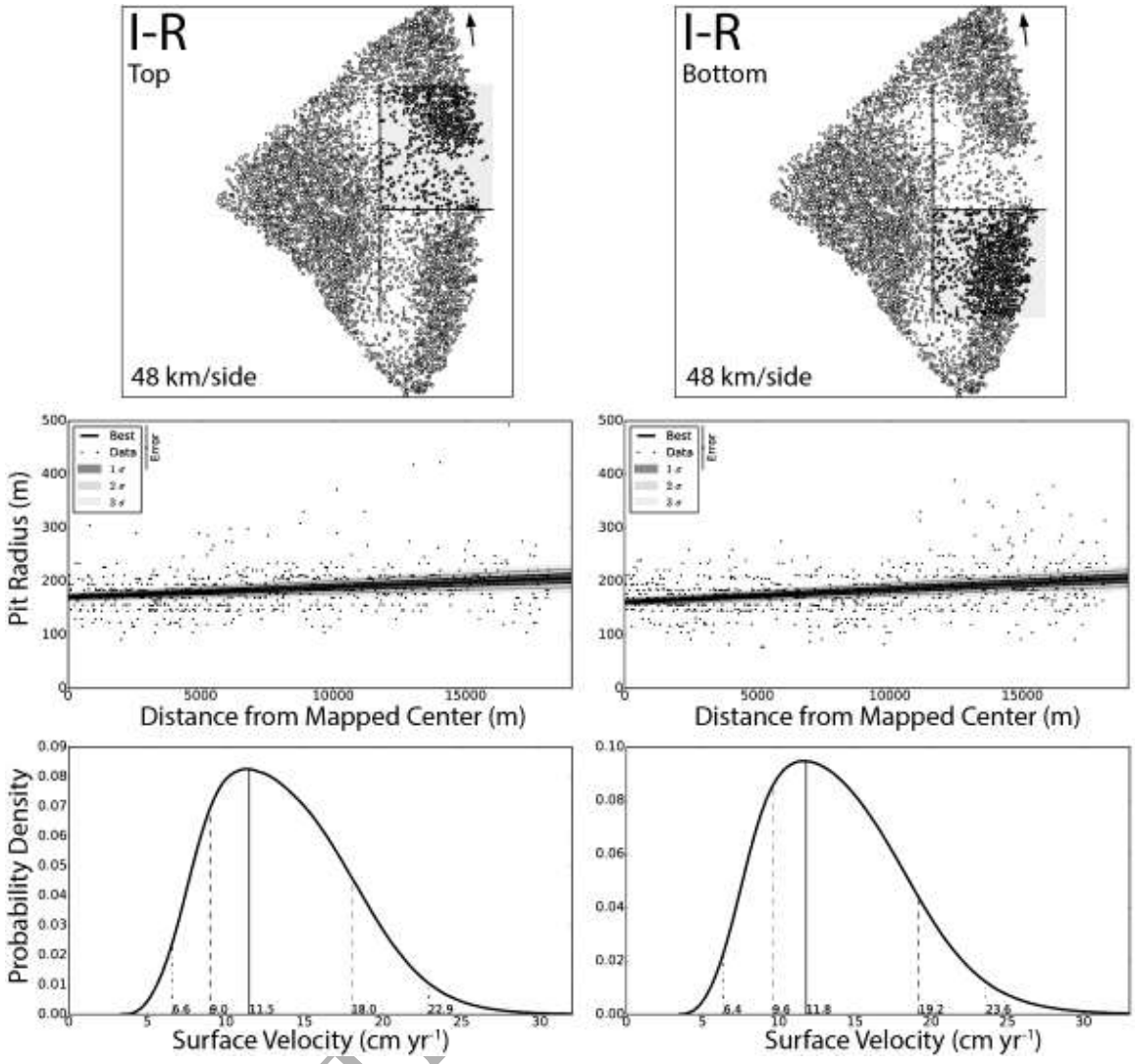

Figure 11. Fits to the upper and lower halves of the right side of cell I, in the same style as Figs. 3, 4, and 7.

Table 1. Cell designations, the number of pits per cell, the cell area, the average number of pits per area, the total area covered by pits, and the total fraction of the cell covered by pits at LORRI resolution.

Cell #	# Pits	Cell Area (km^2)	Average Pits/km^2	Total Pit Area (km^2)	Pit Coverage
I	2889	998	2.9	294	29%
II	1848	659	2.8	220	33%
III	2989	1184	2.5	338	29%
IV	2254	826	2.7	247	30%
V	636	275	2.3	74	27%
VI	354	160	2.2	51	32%
VII	1327	678	2.0	165	24%

Table 2. Map area names corresponding to designations in Figs. 1-4 and 7-9, the number of pits per map area, the best-fit intercept and slope with 68% confidence, the best-fit velocity with 68% and 95% confidence intervals, the length from the spreading center to cell edge, and duration of convection. Values are based on raw data, not accounting for resolution. We only report the number of pits, slope, and intercept for III-L because the other values would be unphysical (see §4.5).

Map Area	# Pits	Intercept (m)	Slope ($m\ m^{-1}$)	Best-fit Velocity ($cm\ yr^{-1}$)	68% Interval ($cm\ yr^{-1}$)	95% Interval ($cm\ yr^{-1}$)	Convection Length (km)	Convection Time (yr)
I-L	1281	158 ± 2	0.00330 ± 0.00025	11.0	8.7-16.9	6.9-21.4	19	1.73E+05
I-R	927	143 ± 3	0.00285 ± 0.00040	13.2	9.7-19.8	7.8-26.8	13	9.85E+04
II-L	1029	128 ± 3	0.00498 ± 0.00021	7.1	5.9-11.3	4.7-14.0	25	3.52E+05
II-R	819	142 ± 3	0.00570 ± 0.00036	6.3	5.0-9.7	4.1-12.4	17	2.70E+05
III-L	1361	185 ± 3	-0.00087 ± 0.00033	-	-	-	-	-
III-R	1113	159 ± 3	0.00298 ± 0.00028	11.9	9.6-18.8	7.8-24.7	17	1.43E+05
IV-L	1049	170 ± 3	0.00214 ± 0.00039	17.9	12.8-26.8	9.8-37.9	13	7.26E+04
IV-R	897	158 ± 3	0.00307 ± 0.00044	12.2	9.5-19.0	6.8-24.5	13	1.07E+05
V	636	148 ± 5	0.00585 ± 0.00075	6.2	4.8-9.6	3.6-12.5	13	2.10E+05
VI	354	186 ± 8	0.00474 ±	7.3	5.0-12.8	3.4-22.3	8	1.10E+05

			0.00156					
VII	1327	148 ± 3	0.00319 ± 0.00017	11.0	9.0-17.4	7.3-21.8	29	2.64E+05
I-R (top)	424	129 ± 4	0.00324 ± 0.00043	11.5	9.0-18.0	6.6-22.9		
I-R (bot)	503	145 ± 4	0.00318 ± 0.00048	11.8	9.6-19.2	6.4-23.6		
III-L (top)	638	171 ± 3	0.00188 ± 0.00031	15.9	12.3-24.5	9.3-31.3		
III-L (bot)	723	161 ± 3	0.00235 ± 0.00028	19.9	15.5-31.6	11.1-41.1		

Table 3. As in Table 2, but adjusting for resolution. "Preferred velocity" is the range between the best-fit velocity in Tables 2 and 3.

Map Area	**Intercept (m)**	**Slope (m m^{-1})**	**Best-fit Velocity (cm yr^{-1})**	**68% Interval (cm yr^{-1})**	**95% Interval (cm yr^{-1})**	**Convection Time (yr)**	**Preferred Velocity (cm yr^{-1})**
I-L	128 ± 2	0.00608 ± 0.00025	5.8	5.2-9.8	3.8-11.3	3.28E+05	5.8-11.0
I-R	76 ± 3	0.00954 ± 0.00039	3.7	3.1-5.9	2.5-7.3	3.51E+05	3.7-13.2
II-L	81 ± 3	0.00768 ± 0.00020	4.6	3.8-7.3	3.1-9.1	5.43E+05	4.6-7.1
II-R	95 ± 3	0.00998 ± 0.00035	3.6	3.0-5.8	2.3-7.0	4.72E+05	3.6-6.3
III-R	105 ± 3	0.00748 ± 0.00027	4.8	4.1-7.8	3.2-9.4	3.54E+05	4.8-11.9
IV-L	114 ± 3	0.00834 ± 0.00037	4.3	3.8-7.1	2.9-8.6	3.02E+05	4.3-17.9
IV-R	101 ± 3	0.00969 ± 0.00042	3.7	3.2-6.1	2.4-7.2	3.51E+05	3.7-12.2
V	83 ± 5	0.01357 ± 0.00072	2.6	2.2-4.2	1.8-5.3	5.00E+05	2.6-6.2
VI	72 ± 7	0.02344 ± 0.00146	1.5	1.3-2.5	1.0-3.1	5.33E+05	1.5-7.3
VII	129 ± 3	0.00422 ± 0.00017	8.1	7.1-13.6	5.7-17.0	3.58E+05	8.1-11.0

References

Barr, A.C. & Milkovich, S.M., 2008. Ice grain size and the rheology of the martian polar deposits. Icarus, 194, pp. 513-518.

Buratti, B.J., Hofgartner, J.D., Hicks, M.D., Weaver, H.A., Stern, S.A., Momary, T., Mosher, J.A., Beyer, R.A., Verbiscer, A.J., Zangari, A.M. & 7 others, 2017. Global Albedos of Pluto and Charon from LORRI New Horizons Observations. Icarus, 287, pp.207-217.

Dobrovolskis, A.R. & Harris, A.W., 1983. The obliquity of Pluto. Icarus, 55, pp. 231-235.

Durham, W.B., Prieto-Ballesteros, O., Goldsby, D.L. & Kargel, J.S., 2010. Rheological and thermal properties of icy materials. Space Science Reviews, 153(1–4), pp.273–298.

Earle, A.M. & Binzel, R.P., 2015. Pluto's insolation history: Latitudinal variations and effects on atmospheric pressure. Icarus, 250, pp.405–412.

Eluszkiewicz, J., 1991. On the microphysical state of the surface of Triton. Journal of Geophysical Research, 96(91), pp.217–229.

Gladstone, G.R., Stern, S.A., Ennico, K., Olkin, C.B., Weaver, H.A., Young, L.A., Summers, M.E., Strobel, D.F., Hinson, D.P., Kammer, J.A. & 24 others, 2016. The atmosphere of Pluto as observed by New Horizons. Science, 351(6279), pp. aad8866-1 - aad8866-6

Greenstreet, S., Gladman, B. & Mckinnon, W.B., 2015. Impact and cratering rates onto Pluto. Icarus, 258, pp.267–288.

Hansen, C.J. & Paige, D.A., 1996. Seasonal Nitrogen Cycles on Pluto. Icarus, 120(2), pp.247–265.

Ingersoll, A.P., Svitek, T. & Murray, B.C., 1992. Stability of polar frosts in spherical bowl-shaped craters on the Moon, Mercury, and Mars. Icarus, 100(1), pp.40–47.

Kass, R.E. & Raftery, A.E., 1995. Bayes Factors. Journal of the American Statistical Association, 430, pp. 773-795.

McKinnon, W.B., Nimmo, F., Wong, T., Schenk, P.M., White, O.L., Roberts, J.H., Moore, J.M., Spencer, J.R., Howard, A.D., Umurhan, O.M. & 6 others, 2016. Convection in a volatile nitrogen-ice-rich layer

drives Pluto's geological vigour. Nature, 534(7605), pp.82–85.

Melosh, H.J., 1986. Impact cratering : a geologic process. Research supported by NASA. New York, Oxford University Press (Oxford Monographs on Geology and Geophysics, No. 11), ch. 9.

Moore, J.M., McKinnon, W.B., Spencer, J.R., Hoawrd, A.D., Schenk, P.M., Beyer, R.A., Nimmo, F., Singer, K., Umurhan, O.M., White, O.L., and 32 others, 2016a. The geology of Pluto and Charon through the eyes of New Horizons. Nature, 351(6279).

Moore, J.M., Howard, A.D., Umurhan, O.M., White, O.L, Schenk, P.M., Beyer, R.A., McKinnon, W.B., Spencer, J.R., Grundy, W.M., Lauer, T.R. & 7 others, 2016b. Sublimation as a landform-shaping process on Pluto. Icarus, 287, pp. 320-333.

Parmentier, E.M. & Head, J.W., 1981. Viscous relaxation of impact craters on icy planetary surfaces: Determination of viscosity variation with depth. Icarus, 47, pp. 100-111.

Protopapa, S., Grundy, W. M., Reuter, D. C., Hamilton, D. P., Ore, C. M., Dalle, Cook, J. C., Cruikshank, D. P., Schmitt, B., Philippe, S. & 13 others, 2017. Pluto's global surface composition through pixel-by-pixel Hapke modeling of New Horizons Ralph/LEISA data. Icarus, 287, pp. 218-228.

Scott, T.A., 1976. Solid and liquid nitrogen. Physics Reports, 27(3), pp.89–157.

Solomon, S.C., Comer, R.P. & Head, J.W., 1982. The Evolution of Impact Basins: Viscous Relaxation of Topographic Relief. Journal of Geophysical Research, 87(B5), pp.3975–3992.

Stansberry, J.A., Pisano, D.J. & Yelie, R. V, 1996. The emissivity of volatile ices on Triton and Pluto. Planetary and Space Science, 44(9). pp. 945-955

Stern, S A., Bagenal, F., Ennico, K., Gladstone, G.R., Grundy, W. M., McKinnon, W.B., Moore, J.M., Olkin, C.B., Spencer, J.R. & 142 others, 2015. The Pluto system: Initial results from its exploration by New Horizons. Science, 350(6258).

Stern, S.A., Binzel, R.P., Earle, A.M., Singer, K.N., Young, L.A., Weaver, H.A., Olkin, C.B., Ennico, K., Moore, J.M., McKinnon, W.B. & 2 others. Past epochs of significantly higher pressure atmospheres on

Pluto. Icarus, 287, pp. 47-53.

Trowbridge, A.J., Melosh, H.J., Steckloff, J.K. & Freed, A.M., 2016. Vigorous convection as the explanation for Pluto's polygonal terrain. Nature, 534(7605), pp.79–81.

Umurhan, O.M., Howard, A.D., Moore, J.M., Earle, A.M., White, O.L., Schenk, P.M., Binzel, R.P., Stern, S.A., Beyer, R.A., Nimmo, F., & 5 others, 2017. Modeling glacial flow on and onto Pluto's Sputnik Planitia. Icarus, 287, 301-319.

Weaver, H. A., Gibson, W.C., Tapley, M.B., Young, L. A. & Stern, S.A., 2008. Overview of the New Horizons Science Payload. Space Science Review, 140, pp.75–91.

Weertman, J., 1970. The creep strength of the Earth's mantle. Reviews of Geophysics, 8(1), pp.145–168.

White, O.L., Moore, J.M., McKinnon, W.B., Spencer, J.R., Howard, A.D., Schenk, P.M., Beyer, R.A., Nimmo, F., Singer, K.N., Umurhan, O.M. & 15 others, 2017. Geological mapping of sputnik planitia on pluto. Icarus, 287, pp. 261-286.

Yamashita, Y., Kato, M. & Arakawa, M., 2010. Experimental study on the rheological properties of polycrystalline solid nitrogen and methane: Implications for tectonic processes on Triton. Icarus, 207(2), pp.972–977.

Zent, A.P., McKay, C.P., Pollack, J.B., Cruikshank, D.P., 1989. Grain Metamorphism in Polar Nitrogen Ice on Triton. Geophysical Research Letters, 16(8), pp.965–968.